



The performance of intermediate temperature solid oxide fuel cells with sputter deposited $\text{La}_{1-x}\text{Sr}_x\text{CoO}_3$ interlayer

A. A. Solovyev^{1,2} · A. V. Shipilova¹ · I. V. Ionov¹ · E. A. Smolyanskiy³ · A. V. Nikonov⁴ · N. B. Pavzderin⁴

Received: 1 July 2020 / Accepted: 1 February 2021 / Published online: 8 February 2021

© The Author(s), under exclusive licence to Springer Science+Business Media, LLC part of Springer Nature 2021

Abstract

The paper studies the performance of the intermediate temperature solid oxide fuel cells with the sputter deposited $\text{La}_{1-x}\text{Sr}_x\text{CoO}_3$ (LSC) interlayer between the cathode and electrolyte. The sputter deposition of the LSC thin films is carried out in argon gas and in a mixture of argon and oxygen gases and then are annealed at 600, 800 and 1000 °C in air for 2 h. The structure and composition of the sputter deposited LSC films are investigated by the X-ray diffraction analysis, scanning and transmission electron microscopies, and energy-dispersive X-ray spectroscopy. The polarization resistance of the sputter deposited LSC films (600 nm thick) on the symmetric cells is 0.13, 0.45 and 2.48 $\text{Ohm}\cdot\text{cm}^2$ measured at 800, 700 and 600 °C, respectively. Measurements are performed by electrochemical impedance spectroscopy. The maximum power density of the anode-supported solid oxide fuel cells with the yttria-stabilized zirconia/gadolinia-doped ceria bilayer electrolyte, LSC interlayer, and LSC cathode is 2.27, 1.58 and 0.68 W/cm^2 measured at 800, 700 and 600 °C, respectively. These values of the power density are respectively 1.4, 1.6 and 2.3 times higher than that of the reference cell without the LSC interlayer.

Keywords SOFC · LSC interlayer · Sputtering · Polarization resistance

1 Introduction

Today, there is a growing interest in the development of solid oxide fuel cells (SOFCs) as one of the most promising energy sources. The development routes in the field include the exploration of multilayer thin-film SOFCs. Conventionally, SOFCs operate at high temperatures (over 800 °C) to ensure the sufficient oxygen ionic conductivity of electrolyte and the catalytic activity of electrodes. The apparent advantage of SOFCs with thin-film electrolytes is the ability to operate within the intermediate temperature range from 600 to 800 °C [1, 2]. This ability decreases the degradation rate,

extends the choice of materials for SOFC components (interconnects and sealing materials) capable of withstanding multiple thermochemical and redox cycles. Another problem arises at lower operating temperatures, which is associated with lower rates of the electrode reaction and, as a consequence, increased polarization loss in the cell. Chemical and electrochemical losses on the cathode cause the cathode resistance, which contributes much to the total resistance of the anode-supported SOFCs [3]. The SOFC efficiency can be enhanced through the application of the novel cathode materials providing the increased catalytic activity for the oxygen reduction reaction or the improvement of cathode structure made of traditional materials.

In most cases, the porous layers of composite materials are used as SOFC electrodes. And the polarization loss can be reduced by the expansion of the triple phase boundary due to the optimized electrode composition and microstructure [4]. Another approach to creating active electrodes is a search for the appropriate materials with mixed ionic-electronic conductivity (MIEC). In this case, there is no need to create a composite in order to get a low polarization resistance. The mixed ionic-electronic conducting materials with fast oxygen diffusion and improved surface kinetics, such as perovskite oxide $\text{La}_{0.6}\text{Sr}_{0.4}\text{CoO}_{3-\delta}$ (lanthanum strontium cobaltite, LSC) [5], increase the oxygen reduction reaction rate. The

✉ A. A. Solovyev
andrewsol@mail.ru

¹ The Institute of High Current Electronics SB RAS, Tomsk, Russia, 2/3, Akademicheskyy Ave, Tomsk 634055, Russia

² The Institute of Solid State Physics RAS, Chemogolovka, 2 Academician Ossipyan Str, Moscow District 142432, Russia

³ National Research Tomsk Polytechnic University, 30, Lenin Ave, Tomsk 634050, Russia

⁴ Institute of Electrophysics of the Ural Division RAS, 106, Amundsen Str, Ekaterinburg 620016, Russia

approaches utilizing a thin and dense MIEC interlayer that forms on the cathode side in addition to the main porous cathode layer, demonstrate good results.

In works [6–8], it was found that even dense MIEC cathodes could possess low polarization resistance. Yoon et al. [9] used pulsed laser deposition to produce a $(\text{La}_{0.5}\text{Sr}_{0.5}\text{CoO}_3)_{0.5}(\text{Ce}_{0.9}\text{Gd}_{0.1}\text{O}_{1.95})_{0.5}$ thin layer of the vertically aligned nanocomposite structure at the cathode/electrolyte interface, and significantly improved the SOFC performance. The increase was identified for the contact area, and the strong reduction in the activation overpotential was observed at the cathode/electrolyte interface. As a result, the maximum power density of the single fuel cell increased by 2 or 3 times at 550–700 °C. Hildenbrand et al. [10, 11] reported that the dense $\text{La}_{0.6}\text{Sr}_{0.4}\text{Co}_{0.2}\text{Fe}_{0.8}\text{O}_3$ cathode layer between the electrolyte and porous cathode reduced the area specific resistance by 30%. Using the pulsed laser deposition technique, they prepared layers 200–2000 nm thick and then tested them on a cell with symmetrical electrodes. Molin et al. [12] used the spray pyrolysis method to deposit thin $\text{LaNi}_{0.6}\text{Fe}_{0.4}\text{O}_3$ -based cathode layers. Symmetric and fuel cell testing demonstrated the improved electrochemical performance of the cathode, as evidenced by the lower area specific resistance and the higher power density.

Such techniques as a pulse laser deposition [9], atomic layer deposition [13], sol-gel deposition [14], electrospraying [15] are successfully used for the formation of the thin-film cathodes based on mixed ionic-electronic conducting materials. One of the most promising is the magnetron sputtering technique. It provides the formation of thin anode films with nanoscale pores and grains [16, 17]. Multicomponent coatings can be obtained by sputtering either one composite target or several single-component targets simultaneously. The advantages of this technique include the coating deposition onto a large-area substrate and reproducibility of results [18]. The main weakness of the sputter deposition process is the high cost of equipment. Nevertheless, a recent cost analysis shows that the high efficiency of sputter deposited SOFCs and the high reproducibility of results can reduce the production costs [19]. Sputter deposited fuel cells manifest a 50% increase in their power density as compared to cells fabricated by conventional techniques such as tape casting, screen printing and firing. The increased power density reduces the number of repeat units necessary for the production of the fuel cell stacks. As a result, the cost of the latter decreases by 33%.

In this work, the sputter deposition is used to produce the LSC interlayer between the yttria-stabilized zirconia (YSZ)/gadolinia-doped ceria (GDC) bilayer electrolyte and the LSC porous cathode contact layer. The LSC interlayer is used due to its mixed ionic-electronic conductivity and high electrocatalytic activity towards the oxygen reduction reaction [20].

Ringuédé et al. [21] and Bieberle-Hüter et al. [22] reported on radiofrequency (RF) magnetron sputter deposition of the

LSC films onto the YSZ pellets and examined the characteristics obtained. They, however, focused only on the LSC film conductivity and microstructure, while no less interesting was the effect of sputter deposited LSC thin films on the SOFC performance. Moreover, the RF sputtering systems (13.56 MHz) were rather complex and difficult for scale applications. In our early research, we showed that such industry-oriented technology as pulsed mid-frequency magnetron sputtering could be used to synthesize the LSC films [23]. That was because the electronic conductivity of the LSC thin film was sufficient for sputtering at medium frequencies (10–250 kHz). It was shown that the LSC interlayer improved the SOFC power density, and the optimum thickness (600 nm) of this layer provided the higher power effect.

The aim of this work is to extensively analyze the influence of the film deposition conditions on the phase composition of the LSC interlayer generated by mid-frequency magnetron sputtering, to study the interlayer effect on the polarization resistance of the cathode and SOFC performance.

2 Experimental procedure

2.1 LSC magnetron sputtering

Thin films were fabricated by magnetron sputtering using pulsed DC power for a 72-mm diameter and 3-mm thickness $\text{La}_{0.6}\text{Sr}_{0.4}\text{CoO}_3$ target (Nova Fabrica Ltd., Lithuania). Silicon wafers, GDC disks (refer to Section 2.3), and anode-supported half-cells with YSZ/GDC electrolyte (refer to Section 2.4) were used as substrates. The base pressure in the evacuated vacuum chamber was 0.01 Pa. Prior to the film deposition, the substrate surface was subjected to the ion beam pre-cleaning. The LSC films were deposited at room temperature, 200 W discharge power, and 80 kHz pulsed DC frequency. The distance between the target and the substrate was 50 mm. Two working atmospheres were used, namely: a pure argon atmosphere at a 0.8 Pa pressure and 100 sccm flow rate, and an argon-oxygen gas mixture at a 1.1 Pa pressure and flow rates of 100 and 70 sccm for argon and oxygen, respectively.

It is known that in oxide cathode sputtering, oxygen can be partially lost during the transport of sputtered atoms to the substrate [24]. Thus, in order to obtain the film composition close to stoichiometric, it is expedient to add oxygen to the working atmosphere. In the pure argon atmosphere, the LSC film deposition rate is 33 nm/min. When oxygen is added to the chamber atmosphere, the film growth rate reduces to 19 nm/min.

Bieberle-Hüter et al. [22] also sputtered the LSC target in the argon-oxygen gas mixture, however, due to a low discharge power (25 W), the deposition rate was very low (0.55 nm/min).

2.2 Characterization

The phase composition of the LSC films was investigated on a Shimadzu XRD-6000 Diffractometer using Cu K_{α} radiation and grazing incidence X-ray diffraction. The operating parameters for the XRD-6000 included 0.03° scan step, $10\text{--}80^{\circ}$ range for angles to be scanned, 40 kV voltage and 30 mA current. The analysis of the phase composition and crystallographic properties of the deposited films was performed using the database of powder diffraction patterns of the International Centre for Diffraction Data (ICDD), Denver, USA, the PCPDFWIN program to view the powder diffraction files (PDF-2), and the PowderCell 2.4 program.

The thickness and microstructure of the LSC films were studied on a JSM-5910LV (JEOL, Japan) scanning electron microscope (SEM). A Solver P47 atomic force microscope (AFM) (NT-MDT Spectrum Instruments, Russia) was used to analyze the surface morphology and the roughness of the film deposited. Observations of the microstructure on thin films were made on a JEM-2100 (JEOL, Japan) transmission electron microscope (TEM) at a 200 keV accelerating voltage. Bright-field and dark-field images and selected area electron diffraction (SAED) images of the as-prepared specimens were acquired. The coated silicon substrate was adhered to an ordinary aluminum workpiece using epoxide resin. The ion slicer EM-09100IS system (JEOL, Japan) was used to prepare the thin films.

2.3 Polarization resistance measurements

Symmetric fuel cells with the GDC electrolyte were prepared to measure the cathode polarization resistance. The commercial powder $\text{Ce}_{0.9}\text{Gd}_{0.1}\text{O}_{2-\delta}$ (Kceracell Co., Ltd., Korea) was used to fabricate the electrolyte specimens. The GDC discs with the diameter of 9 mm and 1 mm thickness were obtained by the static pressing technique. The specimens were sintered at 1600°C for 10 h. After sintering, the density of the obtained specimens was 6.6 g/cm^3 . The LSC electrodes 600 nm thick were sputter-deposited onto both sides of specimens. The active electrode area was 0.5 cm^2 . The electrode polarization resistance was measured by installing the specimens in a measuring cell, in which they were clamped between platinum grids serving as current and potential probes. For the contact homogeneity, the electrode surface was covered with the $\text{La}_{0.6}\text{Sr}_{0.4}\text{CoO}_3$ paste (CERA-FC Co., Korea) layer $\sim 50\text{ }\mu\text{m}$ thick. After an 800°C annealing for 2 h, the polarization resistance was measured in the temperature range of $600\text{--}800^{\circ}\text{C}$ at a 50°C interval. The temperature exposure at each measuring interval was at least 1 h. The impedance spectra were taken at open circuit potential in air using a Solartron SI-1260/1287 impedance meter and a two-electrode configuration. The analysis was conducted at 15 mV input signal amplitude, within a 0.1–1 MHz frequency range.

2.4 Fuel cell preparation and testing

Single fuel cells with a diameter of 20 mm were manufactured to study their electrochemical properties. A fuel cell consisted of the NiO/YSZ anode supports (Ningbo SOFCMAN Energy Technology Co., Ltd., China) with the sputter deposited YSZ ($4\text{ }\mu\text{m}$)/GDC ($2\text{ }\mu\text{m}$) bilayer electrolyte and a $1 \times 1\text{ cm}^2$ LSC interlayer 600 nm thick. The schematic configuration of the single fuel cell is illustrated Fig. 1. In our early research [25], we described in detail the fabrication process of the YSZ/GDC bilayer electrolyte. A $1 \times 1\text{ cm}^2$ LSC cathode contact layer $20\text{ }\mu\text{m}$ thick was formed on the LSC interlayer surface by applying the $\text{La}_{0.6}\text{Sr}_{0.4}\text{CoO}_3$ paste using screen printing. This contact layer improved the contact between the LSC interlayer and the Ag current collector mesh. The contact layer was sintered in-situ, during a 1-h fuel cell exposure to 800°C .

Electrochemical testing of the manufactured fuel cells was carried out on a ProboStat™ system (NORECS, Norway). The current-voltage and current-power characteristics of the fuel cells were measured in the temperature range from 600 to 800°C using a P150 4-electrode potentiostat (Elins Ltd., Russia). Ag and Ni mesh current collectors were used for the cathode and anode, respectively. Dry hydrogen and air were supplied to the anode and cathode chambers at 180 and 400 sccm feed rate, respectively.

3 Results and discussions

The phase composition of the LSC films is analyzed by the X-ray diffraction (XRD) patterns after their deposition on the anode-supported half-cells comprising YSZ/GDC electrolyte followed by 600, 800 and 1000°C annealing to achieve the desired LSC crystal phases. The XRD patterns of $1\text{-}\mu\text{m}$ thick LSC films deposited in argon and argon-oxygen gas mixture are shown in Fig. 2, which also indicates the corresponding compounds and crystallographic orientations. The XRD peaks corresponding to the underlying GDC layer are observed for all the specimens. Dashed lines indicate the diffraction peaks of rhombohedral $\text{La}_{0.6}\text{Sr}_{0.4}\text{CoO}_{3-\delta}$ [26] and cubic $\text{Ce}_{0.9}\text{Gd}_{0.1}\text{O}_2$ (the ICDD PDF-2 database file number for this

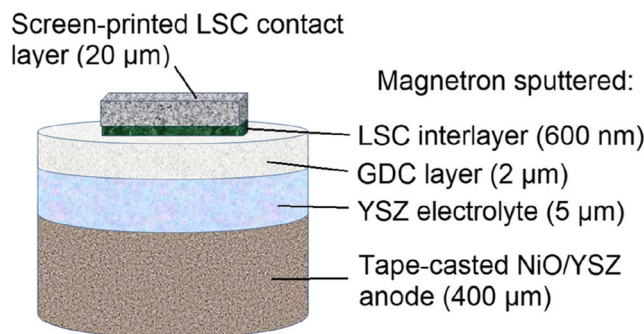


Fig. 1 Schematic configuration of the single fuel cell

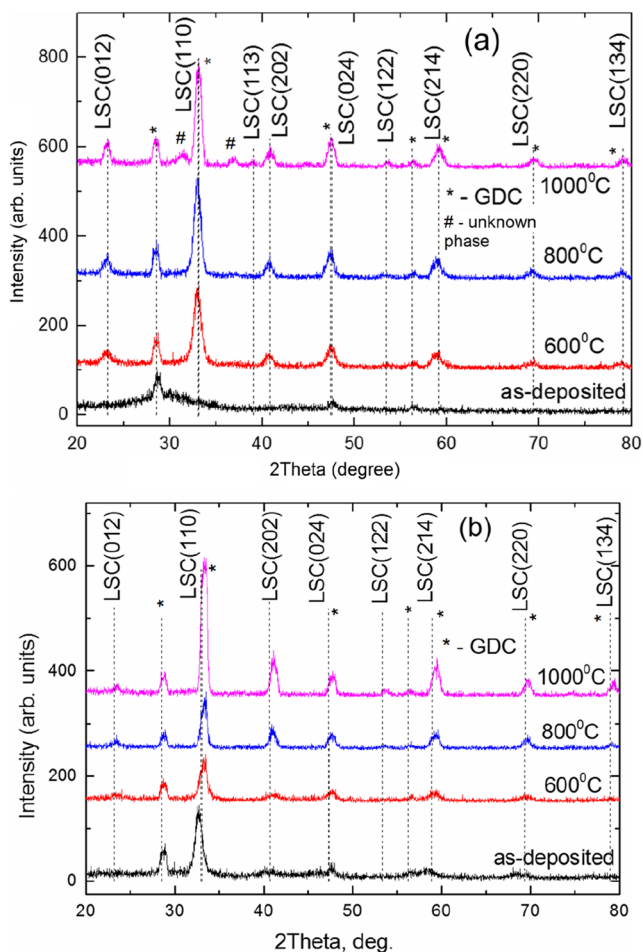


Fig. 2 XRD patterns of as-deposited LSC films and after 600, 800 and 1000 °C annealing in air: *a* – in Ar gas, *b* – in Ar + O₂ mixture

phase is 04–012–3418) structures given for comparison. The XRD pattern obtained for the film deposited in argon without annealing has no LSC diffraction peaks. This may imply an amorphous state of the film. The amorphous film state can be explained by the low deposition temperature. During the physical vapor deposition, the final atom arrangement in the film depends on the vapor ionization degree, the ion kinetic energy and the substrate temperature. The formation of the amorphous film denotes a lack of thermal energy during the physical vapor deposition, whereas this energy is required for the atomic rearrangement into the lowest-energy configuration. The LSC peaks, however, appear after 600 °C annealing, and their intensity increases with annealing temperature. It means that the thermal treatment does improve the film crystallinity. Despite this fact, it is not easy to differentiate between the LSC and GDC peaks, because most of them overlap each other. However, we observe several LSC peaks, for example, (012) and (202), that do not coincide with the GDC phase.

The XRD pattern shown in Fig. 2b for the LSC film as-deposited in the Ar + O₂ mixture, has a small peak at $2\theta = 41^\circ$

and a pronounced peak at $2\theta = 33^\circ$, which most likely belong to the LSC crystalline phase. Moreover, for the films deposited in the Ar + O₂ mixture with successive annealing, the LSC peaks shift towards the higher diffraction angles, implying the internal stress formation in the films. Thus, the oxygen addition to the working atmosphere affects the crystalline structure of the LSC films. The microstructure and stresses in the vacuum-deposited films are sensitive to the deposition conditions. The shift of the LSC peaks towards higher diffraction angles observed for the films deposited in the Ar + O₂ mixture, can be probably explained by the following factors. First of all, when oxygen is added to the argon atmosphere, the metal atoms sputtering from the target react with oxygen, causing changes in the film growth kinetics. In the oxygen-rich environment, the oxygen atom tends to occupy the interstitial site, resulting in the compressive stress formation in the films [27]. Secondly, the negative oxygen ion bombardment of the growing films affects the film microstructure. Tominaga et al. [28] observe high-energy negative oxygen ions appeared in the target erosion zone. The growing film bombardment by high-energy oxygen ions (O⁻) accelerating at the cathode fall, can vary the film properties and structure [29].

The diffraction peaks of an unknown phase are detected after 1000 °C annealing for the film deposited in pure argon.

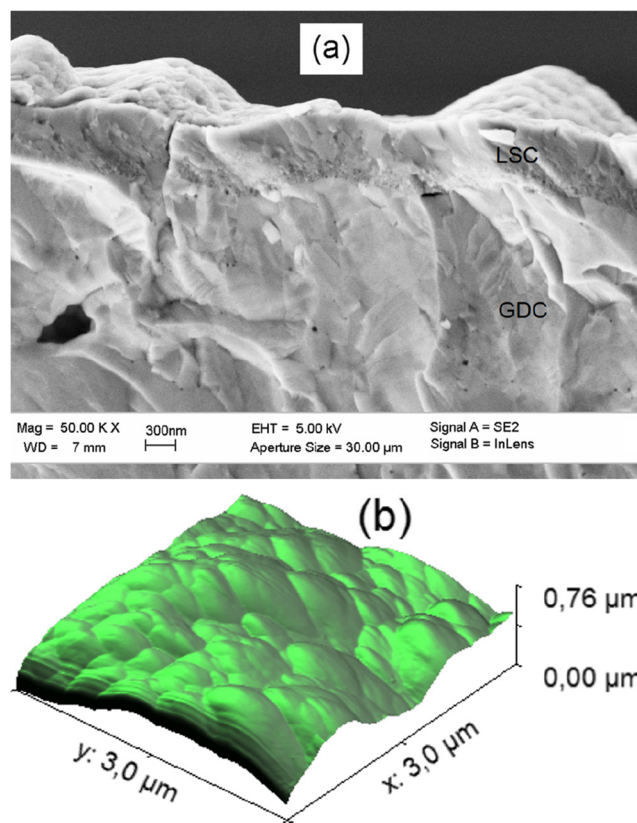
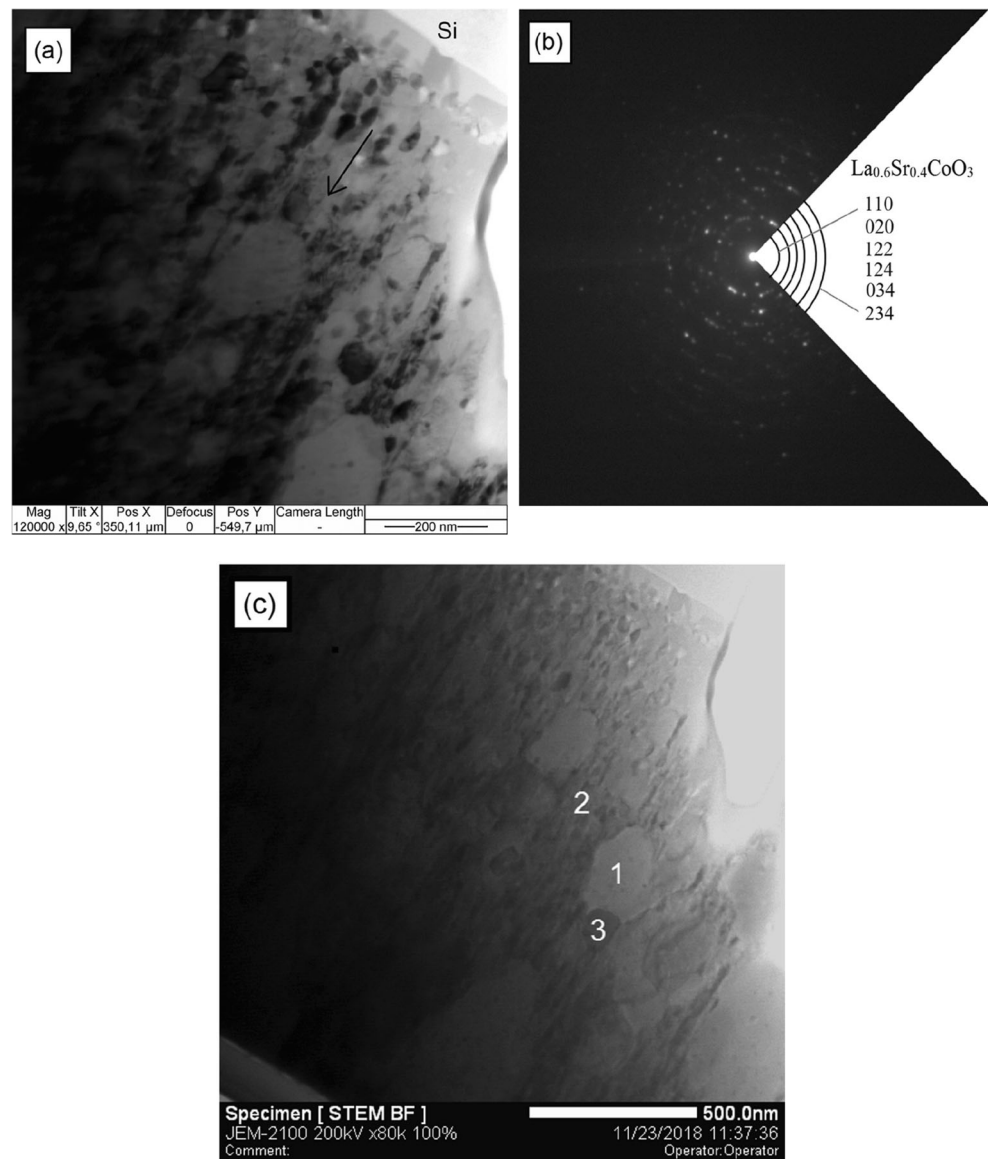


Fig. 3 Cross-sectional SEM image of the magnetron sputtered LSC film (a) and 3D AFM image of the LSC film surface (b)

Fig. 4 Cross-sectional bright-field TEM image (a); SAED pattern (b); STEM image (c) of the LSC film deposited onto Si substrate



We therefore will carefully analyze only the films after the successive 800 °C annealing.

SEM observations are used to characterize the microstructure of the LSC film and the cathode/electrolyte interface. Figure 3(a) shows the cross-sectional SEM image of the 700-nm thick LSC film deposited in the argon-oxygen mixture and annealed at 800 °C in air. The film demonstrates a relatively dense nanocrystalline structure and good contact with the GDC electrolyte layer. Figure 3(b) contains a 3D AFM image of the LSC film surface with the average grain size of about 220 nm. The root-mean-square roughness of a $3 \times 3 \mu\text{m}$ area is 12 nm.

Figure 4(a) presents a typical cross-sectional bright-field TEM image of the LSC film 1.7 μm thick deposited in the Ar + O₂ mixture onto the silicon substrate. The film is exposed to 800 °C annealing in air for 2 h. Black arrow indicates the

direction of the film growth. Its structure is nanocolumnar, with embedded, relatively large (200–400 nm) crystallites. This is shown in both the bright-field TEM and the scanning transmission electron microscopy (STEM) images given in

Table 1 Chemical composition of LSC film determined by EDX spectroscopy at points 1–3 indicated in Fig. 4(c)

	Chemical composition (at.%)			
	O	Co	Sr	La
Point 1	66.83	16.54	3.64	12.99
Point 2	65.75	16.90	3.91	13.44
Point 3	63.84	17.45	4.22	14.49

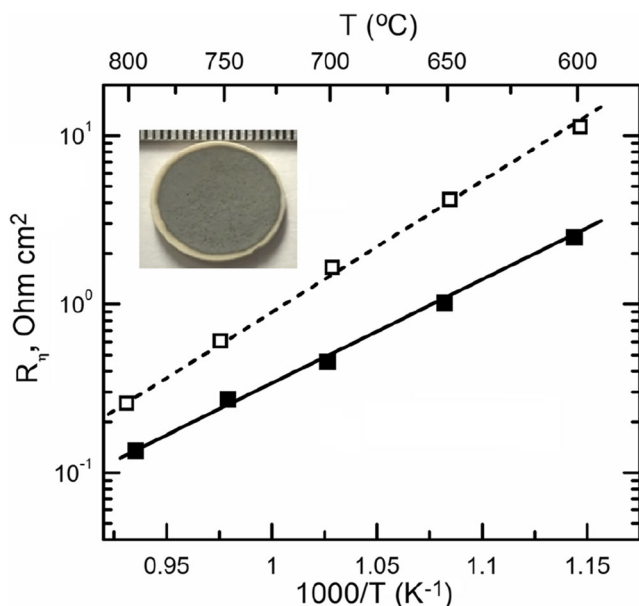
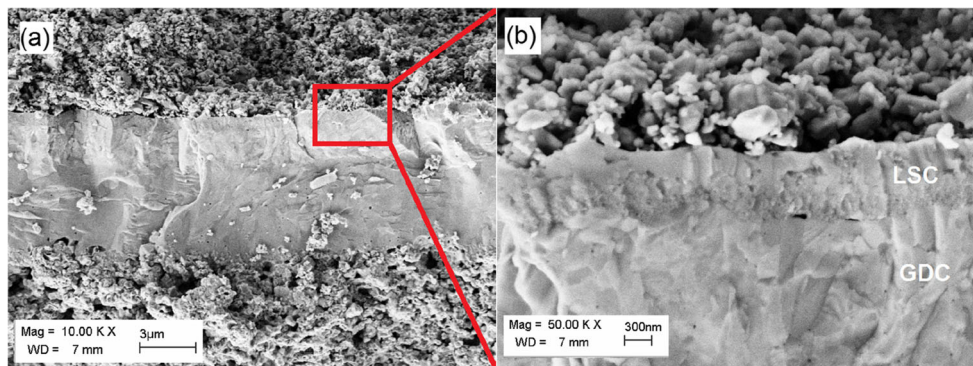


Fig. 5 Temperature dependencies of cathode polarization resistance of symmetrical cell with LSC interlayer (closed symbols) and without it (open symbols). Inset: photograph of the LSC interlayer on the GDC disc

Fig. 4(c). The SAED pattern presented in Fig. 4(b) indicates to the LSC film crystallinity. The well-defined diffraction spots of the LSC film can be distinguished by the regular spacing expected for a rhombohedral lattice. The LSC film shows the diffraction patterns resembling polycrystalline material with only slightly preferred (020) orientation, which confirms the XRD patterns in Fig. 2.

The energy dispersive X-ray analysis of the chemical composition carried out for points 1–3 indicated in Fig. 4c, shows no significant deviations in the crystallites. As can be seen from Table 1, the sputter deposition results in strontium-deficient layers. The same is observed in the RF magnetron sputtered LSC films obtained by Bieberle-Hütter and Tuller [22]. At the nominal $\text{La}_{0.5}\text{Sr}_{0.5}\text{CoO}_3$ target composition, the composition of their films measured by Rutherford backscattering spectroscopy, was $\text{La}_{0.84}\text{Sr}_{0.16}\text{Co}_{0.67}\text{O}_x$. In our further research, we intend to eliminate the strontium deficiency in the film by increasing its content in the sputtered target.

Fig. 6 Cross-sectional SEM images obtained after cell testing: (a) NiO/YSZ anode support, YSZ (4 μm) / GDC (2 μm) bilayer electrolyte, LSC interlayer and LSC cathode, (b) enlarged image of the selected area in Fig. 6(a)



The electrochemical impedance spectroscopy (EIS) technique was used to measure the polarization resistance of the LSC films by the electrical response of symmetrical LSC electrodes on the GDC electrolyte. EIS was conducted within the air temperature range of 600–800 °C. The impedance spectra were obtained at the open-circuit voltage. The cathode area-specific resistance (ASR) was calculated as $\text{ASR} = R_{\eta} \cdot A / 2$, where R_{η} is the polarization resistance at the cathode/electrolyte interface, and A is the active area (1 cm^2) [30].

Figure 5 shows the temperature dependencies of the cathode polarization resistance R_{η} of the symmetrical cells with and without the LSC interlayer. The polarization resistance of 0.13 and 2.48 $\Omega \text{ cm}^2$ is obtained at temperature of 800 °C and 600 °C, respectively. Since the contact layer also contributes to the cathode polarization resistance, measurements are made for the symmetrical cell without the LSC interlayer. According to Fig. 5, the cathode polarization resistance is much higher without the LSC interlayer. At the same time, the lower the temperature, the greater the difference between the polarization resistance of the symmetrical cells.

The investigation of the electrochemical performance of the sputter deposited LSC interlayer included the cell fabrication and testing. For comparison, the reference cell without the LSC interlayer was produced. Figure 6 contains the cross-sectional SEM images of the cell prepared as described in Section 2. These images were obtained after the cell testing. According to Fig. 6, all the three layers (YSZ, GDC, and LSC) deposited by magnetron sputtering in Ar + O₂ mixture adhered properly to each other and to the anode substrate they were deposited on. No crack, lamination or other defects were found even after electrochemical cell testing.

The performance of single cells with the LSC interlayer sputtered in Ar and Ar + O₂ mixture are compared with that of the reference cell (without the LSC interlayer). As shown in Fig. 7(a), the reference cell demonstrates the open-circuit voltage in the range of 1.06–1.11 V, depending on temperature which is close to the theoretical value. This confirms the formation of the fully dense electrolyte and gas permeability of the cells achieved during their testing. The cells with the LSC interlayer have a lower open-circuit voltage (1.04–1.07 V)

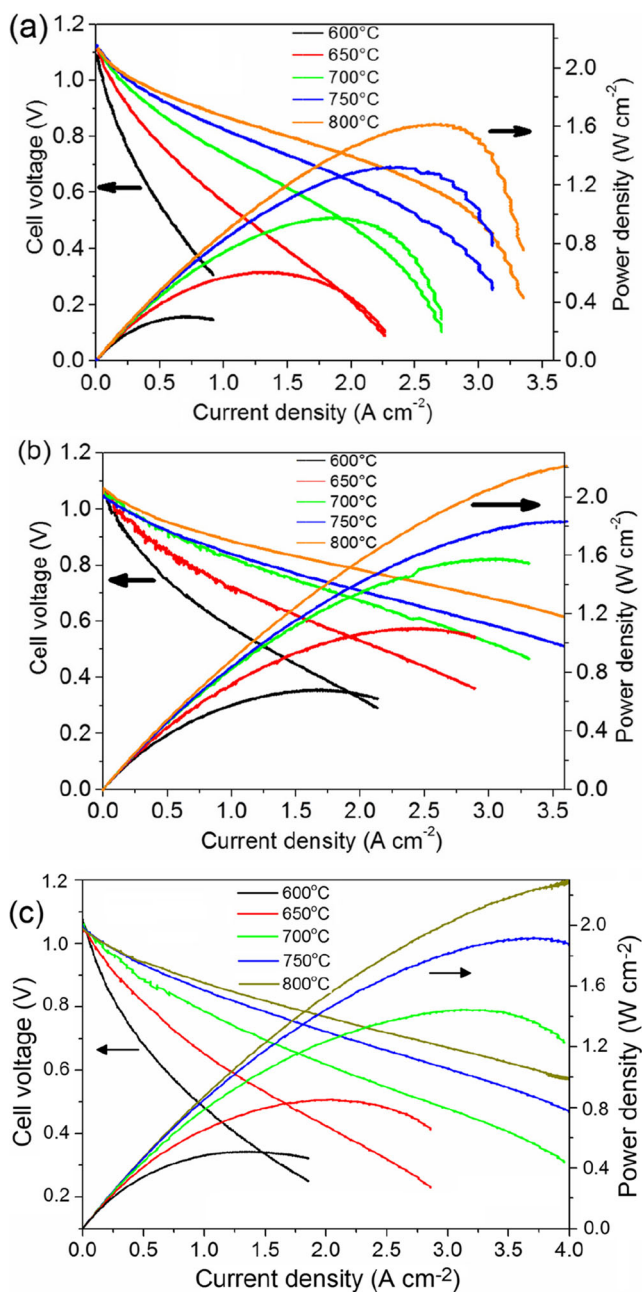


Fig. 7 Cell voltage and power density of anode-supported single cells at different temperatures (600–800 °C): *a* – without interlayer, *b* – with LSC interlayer deposited in Ar, *c* – with LSC interlayer deposited in Ar + O₂ mixture

despite the identity of the cell electrolyte. But these cells also have lower activation losses, as shown in Fig. 7(b), (c) on the current density-voltage curves at a low (<0.5 A/cm²) current density. Since the anode of the compared cells is also identical, the activation loss decrease can be associated only with the presence of the LSC interlayer.

Electrochemical testing indicates that in the whole temperature range, the power density of the fuel cells with the LSC interlayer is higher than in the cell without it. This is consistent with measurements of the cathode polarization resistance. For

example, the maximum power densities of 2.27, 1.58 and 0.68 W/cm² are obtained for the cell with the LSC interlayer deposited in argon at 800, 700 and 600 °C, respectively. These values are 1.4, 1.6 and 2.3 times higher than that obtained for the reference cell in the same temperature range. The maximum power densities of 2.29, 1.45 and 0.51 W/cm² are obtained the cell with the LSC interlayer deposited in the Ar + O₂ mixture at 800, 700 and 600 °C, respectively. The LSC layers deposited in different atmospheres operate in approximately the same way. This is consistent with the fact that their phase composition slightly differs. The advantage of the cells with the LSC interlayer grows with decreasing operating temperature. The obtained values of the maximum power density exceed the values reached in works [31] (0.54 W/cm² power density at 700 °C) and [32] (0.412 W/cm² power density at 700 °C) for the anode-supported SOFC made of the same materials having the cell compositions of NiO-YSZ|YSZ|GDC|LSC70:GDC30 and NiO-YSZ|YSZ|GDC|LSC, respectively.

The ASR of the reference cell measured in the linear part of the current-voltage characteristic at 800 °C, equals 0.15 Ohm·cm², which is 1.5 times higher than 0.1 Ohm·cm² ASR for both cells with the LSC interlayer. This means a significant decrease in the internal resistance, particularly, ohmic resistance in cells with the LSC interlayer.

The thin and dense interlayer between the cathode and the electrolyte of the SOFC made of mixed ionic-electronic conducting materials, provides the following positive consequences. Firstly, it serves as a mechanical-structural function and enhances the interfacial adhesion between the porous cathode and the electrolyte. Secondly, it decreases the mechanical degradation caused by the difference in the thermal expansion coefficients of the electrolyte and cathode layers. Thirdly, the LSC interlayer increases the number of oxygen-ion pathways on the cathode/electrolyte interface. In cells without the LSC interlayer, the oxygen ions penetrate into electrolyte only in contact places, between the cathode granules and the electrolyte surface. Thus, the operation of cathodes with the thin and dense interlayer is more efficient due to the formation of more contact points between the cathode and electrolyte. If the interlayer is made of the cathode material, the oxygen ions can penetrate into the entire electrolyte surface.

4 Conclusion

This study demonstrated that the sputter deposited LSC thin films used as the cathode interlayer for intermediate-temperature solid oxide fuel cells, assisted in the successful achievement of the high-power density. The LSC films were smooth, dense and well adhesive. After 800 °C annealing, their structure became polycrystalline and single-phase. The single cells with the cathode interlayer demonstrated rather a

high power density of ~ 2.3 and ~ 0.5 – 0.6 $\text{W}\cdot\text{cm}^{-2}$ at 800 and 600 °C, respectively. It was found that the power density was enhanced by the better adhesion between the porous cathode and electrolyte, the increase in the oxygen-ion pathways from the cathode to electrolyte, which reduced losses caused by the cathode polarization resistance. That approach, which utilized conventional oxide materials such as YSZ, GDC and LSC and the sputter deposition for the thin films, can be used to produce SOFCs with the superior performance, large area, and high productivity that are very important characteristics of the magnetron sputtering technique.

Acknowledgments This work was supported by Grant No. 17-79-30071 from the Russian Science Foundation. The authors are grateful to the administration of the Institute of Electrophysics of the Ural Division RAS for providing EIS measurements under the government contract No. 0389-2019-0004.

References

- J. Jiang, J.L. Hertz, J. Electroceram. **32**(1), 37–46 (2014). <https://doi.org/10.1007/s10832-013-9857-1>
- J.H. Park, W. Hong, J. Lee, K.J. Yoon, H. Kim, J. Hong, H.-S. Song, J.-W. Son, J. Electroceram. **33**(1-2), 25–30 (2014). <https://doi.org/10.1007/s10832-014-9903-7>
- R. Barfod, A. Hagen, S. Ramousse, P.V. Hendriksen, M. Mogensen, Fuel Cells **6**(2), 141–145 (2006). <https://doi.org/10.1002/fuce.200500113>
- J.H. Park, S.M. Han, B.K. Kim, J.H. Lee, K.J. Yoon, H. Kim, H.I. Ji, J.W. Son, Electrochim. Acta **296**, 1055–1063 (2019). <https://doi.org/10.1016/j.electacta.2018.11.018>
- A.A. Samat, M.R. Somalu, A. Muchtar, O.H. Hassan, N. Osman, J. Sol-Gel Sci. Technol. **78**(2), 382–393 (2016). <https://doi.org/10.1007/s10971-015-3945-4>
- D. Chen, S.R. Bishop, H.L. Tuller, J. Electroceram. **28**(1), 62–69 (2012). <https://doi.org/10.1007/s10832-011-9678-z>
- S. Okada, S. Miyoshi, S. Yamaguchi, ECS Trans. **68**(1), 987–994 (2015). <https://doi.org/10.1149/06801.0987ecst>
- A.V. Nikonov, N.B. Pavzderin, S.N. Shkerin, O.I. Gyrdasova, A.S. Lipilin, Russ. J. Appl. Chem. **90**(3), 369–373 (2017). <https://doi.org/10.1134/S1070427217030077>
- J. Yoon, S. Cho, J.H. Kim, J.H. Lee, Z. Bi, A. Serquis, X. Zhang, A. Manthiram, H. Wang, Adv. Funct. Mater. **19**(24), 3868–3873 (2009). <https://doi.org/10.1002/adfm.200901338>
- B.A. Boukamp, N. Hildebrand, P. Nammensma, D.H.A. Blank, Solid State Ionics **192**(1), 404–408 (2011). <https://doi.org/10.1016/j.ssi.2010.05.037>
- N. Hildebrand, B.A. Boukamp, P. Nammensma, D.H.A. Blank, Solid State Ionics **192**(1), 12–15 (2011). <https://doi.org/10.1016/j.ssi.2010.01.028>
- S. Molin, P.Z. Jasinski, Mater. Lett. **189**, 252–255 (2017). <https://doi.org/10.1016/j.matlet.2016.11.101>
- H.J. Choi, K. Bae, S. Grieshammer, G.D. Han, S.W. Park, J.W. Kim, D.Y. Jang, J. Koo, J.W. Son, M. Martin, J.H. Shim, Adv. Energy Mater. **8**(33), 1802506 (2018). <https://doi.org/10.1002/aenm.201802506>
- L. Dieterle, P. Bockstaller, D. Gerthsen, J. Hayd, E. Ivers-Tiffée, U. Guntow, Adv. Energy Mater. **1**(2), 249–258 (2011). <https://doi.org/10.1002/aenm.201000036>
- S.S. Shin, J.H. Kim, G. Li, S.Y. Lee, J.W. Son, H. Kim, M. Choi, Int. J. Hydrogen Energ. **44**(9), 4476–4483 (2019). <https://doi.org/10.1016/j.ijhydene.2018.11.143>
- F.J. Garcia-Garcia, F. Yubero, A.R. González-Elipé, S.P. Balomenou, D. Tsiplakides, I. Petrakopoulou, R.M. Lambert, Int. J. Hydrogen Energ. **40**(23), 7382–7387 (2015). <https://doi.org/10.1016/j.ijhydene.2015.04.001>
- F.J. Garcia-Garcia, F. Yubero, J.P. Espinós, A.R. González-Elipé, R.M. Lambert, J. Power Sources **324**, 679–686 (2016). <https://doi.org/10.1016/j.jpowsour.2016.05.124>
- H.S. Noh, J. Hong, H. Kim, K.J. Yoon, B.K. Kim, H.W. Lee, J.H. Lee, J.W. Son, J. Electrochem. Soc. **163**(7), F613–F617 (2016). <https://doi.org/10.1149/2.0331607jes>
- M.R. Weimar, L.A. Chick, D.W. Gotthold, G.A. Whyatt, DOE Report, Cost study for manufacturing of solid oxide fuel cell power systems. (United States, 2013). DOI: <https://doi.org/10.2172/1126362>
- J.M. Ralph, A.C. Schoeler, M. Kumpelt, J. Mater. Sci. **36**(9), 1161–1163 (2001). <https://doi.org/10.1007/s10853-008-2502-8>
- A. Ringuedé, J. Fouletier, Solid State Ionics **139**(3-4), 167–177 (2001). [https://doi.org/10.1016/S0167-2738\(01\)00692-0](https://doi.org/10.1016/S0167-2738(01)00692-0)
- A. Bieberle-Hütter, H.L. Tuller, J. Electroceram. **16**(2), 151–157 (2006). <https://doi.org/10.1007/s10832-006-5945-9>
- E.A. Smolyanskiy, S.A. Linnik, I.V. Ionov, A.V. Shipilova, V.A. Semenov, A.L. Lauk, A.A. Solov'yev, J. Phys. Conf. Ser. **1115**, 032080 (2018). <https://doi.org/10.1088/1742-6596/1115/3/032080>
- P. Lippens, U. Muehlfeld Indium Tin Oxide (ITO): Sputter Deposition Processes. In: Handbook of Visual Display Technology. Chen J., Cranton W., Fihn M. (eds). Springer, Berlin, Heidelberg (2012). DOI: https://doi.org/10.1007/978-3-540-79567-4_54
- A.A. Solov'yev, A.V. Shipilova, I.V. Ionov, A.N. Kovalchuk, S.V. Rabotkin, V.O. Oskirko, J. Electron. Mater. **45**(8), 3921–3928 (2016). <https://doi.org/10.1007/s11664-016-4462-0>
- N.M.L.N.P. Closset, R.H.E. van Doorn, H. Kruidhof, Powder Diffraction **11**(1), 31 (1996). <https://doi.org/10.1017/S0885715600008873>
- C.R. Gobbiner, M.A.A. Veedu, D. Kekuda, Appl. Phys. A Mater. Sci. Process. **122**(4), 272 (2016). <https://doi.org/10.1007/s00339-016-9806-3>
- K. Tominaga, S. Iwamura, Y. Shintani, O. Tada, Jpn. J. Appl. Phys. **21**, 688 (1982). <https://doi.org/10.1143/JJAP.21.688>
- H.C. Nguyen, T.T. Trinh, T. Le, C.V. Tran, T. Tran, H. Park, V.A. Dao, J. Yi, Semicond. Sci. Technol. **26**(10), 105022 (2011). <https://doi.org/10.1088/0268-1242/26/10/105022>
- S.A.M. Ali, M. Anwar, N.A. Baharuddin, M.R. Somalu, A. Muchtar, J. Solid State Electrochem. **22**(1), 263–273 (2018). <https://doi.org/10.1007/s10008-017-3754-5>
- Y. Tao, J. Shao, W.G. Wang, J. Wang, Fuel Cells **9**(5), 679–683 (2009). <https://doi.org/10.1002/fuce.200900058>
- Q. Su, D. Yoon, Y.N. Kim, W. Gong, A. Chen, S. Cho, A. Manthiram, A.J. Jacobson, H. Wang, J. Power Sources **218**, 261–267 (2012). <https://doi.org/10.1016/j.jpowsour.2012.06.094>

Publisher's note Springer Nature remains neutral with regard to jurisdictional claims in published maps and institutional affiliations.